https://doi.org/10.1595/205651321X16013966874707 *Johnson Matthey Technol. Rev.*, 2021, **65**, (2), 247–262

JOHNSON MATTHEY
TECHNOLOGY REVIEW

www.technology.matthey.com

# State-of-the-Art Iridium-Based Catalysts for Acidic Water Electrolysis: A Minireview of Wet-Chemistry Synthesis Methods

**Preparation routes for active and durable iridium catalysts**

**Himanshi Dhawan**
Department of Chemical and Materials Engineering, University of Alberta, 12th Floor, Donadeo Innovation Centre for Engineering, 9211 – 116 Street, NW Edmonton, Alberta, T6G 1H9, Canada

**Marc Secanell**
Department of Mechanical Engineering, University of Alberta, 10-203 Donadeo Innovation Centre for Engineering, 9211 – 116 Street, NW Edmonton, Alberta, T6G 1H9, Canada

**Natalia Semagina***
Department of Chemical and Materials Engineering, University of Alberta, 12th Floor, Donadeo Innovation Centre for Engineering, 9211 – 116 Street, NW Edmonton, Alberta, T6G 1H9, Canada

***Email:** semagina@ualberta.ca

With the increasing demand for clean hydrogen production, both as a fuel and an indispensable reagent for chemical industries, acidic water electrolysis has attracted considerable attention in academic and industrial research. Iridium is a well-accepted active and corrosion-resistant component of catalysts for oxygen evolution reaction (OER). However, its scarcity demands breakthroughs in catalyst preparation technologies to ensure its most efficient utilisation. This minireview focusses on the wet-chemistry synthetic methods of the most active and (potentially) durable iridium catalysts for acidic OER, selected from the recent publications in the open literature. The catalysts are classified by their synthesis methods, with authors' opinion on their practicality. The review may also guide the selection of the state-of-the-art iridium catalysts for benchmarking purposes.

## 1. Introduction

Hydrogenations and hydrotreating reactions with molecular hydrogen are critical operations in chemical and related industries. Regardless of the nature of the hydrotreated reactants and products, as society walks away from fossil fuels, the need for hydrogen will remain indispensable. With the increasing access to surplus renewable electricity, the hydrogen production by water electrolysis may take its rightful place not only in transportation and energy storage, but also as a clean hydrogen supply for chemical and related industries (1), replacing greenhouse gas (GHG)-producing methane steam reforming. Among the commercialised and emerging technologies, acidic proton exchange membrane (PEM) electrolysers can operate at up to 20 A $cm^{-2}$ current density and deliver up to 700 bar hydrogen at high efficiencies (2). Active and durable electrocatalysts are required to reduce the power input, the bottleneck being the sluggish anodic OER. The acidic environment, however, demands corrosion-resistant materials at high potentials. The winner so far is the OER-active conductive and corrosion-resistant iridium at typical loadings of 1–2 mg $cm^{-2}$. Lower iridium requirements were demonstrated, for example, for a PEM electrolyser with the 3 M nanostructured thin film (NSTF) catalyst reaching 2 A $cm^{-2}$ current density at 1.86 V at 0.25 $mg_{Ir}$ $cm^{-2}$

(3), which translates into *ca*. 100 tonnes iridium for the production of 1 TW hydrogen (4). It is obvious that with the current technologies, the terawatt-scale hydrogen production cannot be met with the annual supply of scarce iridium of less than 10 tonnes (4). The annual global demand of hydrogen was reported as 73.9 million tonnes in 2018; as it is almost entirely supplied from fossil fuels, its current production emits 830 million tonnes of carbon dioxide per year (5). The hydrogen production replacement in chemical industries with water electrolysis is relatively well-positioned as a target area for decarbonisation of the industrial sector.

Hundreds of research papers have been focussed on the development of active and durable iridium catalysts, deposition techniques and associated catalyst layer components, which may limit the performance of the most active iridium catalyst formulations. Recent reviews classified iridium-containing catalysts for acidic OER (6) and the variety of methods for the synthesis of iridium oxide (7). Commercial catalyst production methods must be scalable, preferably not require specialised equipment apart from what is available in the catalyst production industries, not produce significant waste and lack the need for large amounts of chemicals, especially those that are hazardous to the environment. With this in mind, the objective of the current minireview is to select a number of the most efficient state-of-the-art iridium catalysts for acidic OER within reported wet-chemistry synthesis methods, focussing on the practicality and scalability of the techniques. We address only wet-chemistry routes, as they are most frequently reported, being relatively accessible in a research environment. **Figure 1** and **Table I** summarise the catalyst synthetic routes and selected catalysts, addressed in this review; this is not a comprehensive summary of all possible routes and catalysts, but rather a careful selection of studies demonstrating promising combination of activity and stability in acidic OER.

The catalyst layer preparation methods, such as deposition methods, are out of the scope of this work, although they significantly affect the catalyst performance. Gas-phase catalyst (layer) preparation techniques (13, 14) are omitted for the same reason, as they require specialised equipment and feature simultaneous catalyst formation and its deposition. The review is based only on published research works; we acknowledge that it may become obsolete due to the rapid developments in the field or may miss some critical proprietary information. The citations are chosen only to support our viewpoints; they cannot be considered as a comprehensive list of the relevant works. Herein, we aim to provide comprehensive insights in selected promising wet-synthesis methods. We hope that the review may help the reader in the selection of a state-of-art catalyst for benchmarking purposes, as well as to assist in further developments of potentially scalable synthesis of active and durable iridium catalysts.

## 2. Requirements to the Iridium Catalyst Performance and Structure: Activity *vs*. Stability

Bernt (15, 16) estimated that, in order to decarbonise the transportation sector by

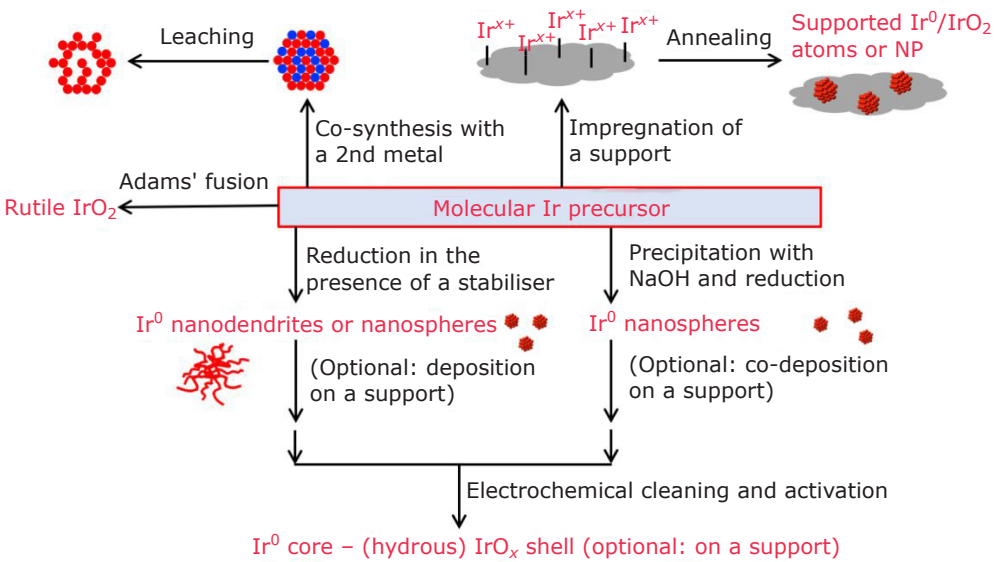


Fig. 1. Summary of the reviewed wet-chemistry synthetic routes of state-of-the-art iridium catalysts for acidic OER

**Table I Summary of the State-of-the-Art Activities of Selected Catalysts Prepared by Wet-Chemistry Synthesis and Tested in a Rotating Disk Electrode**

| Catalyst (method) and section *vide infra* | Loading on the electrode, $mg_{Ir}$ $cm^{-2}$ | Overpotential at 10 mA $cm^{-2}$, mV | Activity | References |
|---|---|---|---|---|
| **3.2 Surfactant-assisted** | 0.061 | ~290 | 100 A $g_{Ir}^{-1}$ at 1.51 $V_{RHE}$ | (8) |
| **3.3 Surfactant-free colloids** | 0.0071 | 345 | 205 A $g_{Ir}^{-1}$ at 1.5 $V_{RHE}$ | (9) |
| **4. Supported on GCN** | 0.07 | 278 | 580 A $g_{Ir}^{-1}$ at 1.55 $V_{RHE}$ | (10) |
| **4. Supported on TaTO** | 0.02 | ~300 | 250 A $g_{Ir}^{-1}$ at 1.51 $V_{RHE}$ | (11) |
| **5.2 Selective leaching** | 0.0277 | N/A | 810 A $g_{Ir}^{-1}$ at 1.51 $V_{RHE}$, 3353 A $g_{Ir}^{-1}$ at 1.55 $V_{RHE}$ | (12) |

Note that the data are mostly reported for the fresh catalysts. Stability data, where available, are discussed in the text

transitioning to fuel cell vehicles fuelled by renewable hydrogen, the metal loadings on the anode of polymer electrolyte water electrolysers should be decreased to 0.05 $mg_{Ir}$ $cm^{-2}$. This loading can meet the demand for approximately 150 GW $year^{-1}$ installed capacity while using only 50% of the annual iridium production. In order to meet this requirement and also use electrolysis for other needs, such as energy storage and chemical industry supply, the specific iridium activity must be increased substantially. An ideal OER catalyst would have negligible overpotential; a highly desirable catalyst would be one that requires 200–300 mV overpotential (1.43–1.53 V) at 10 mA $cm^{-2}$ current, with catalysts achieving this same current density at overpotentials of 300–400 mV (1.53–1.63 V) being acceptable (17). As a durability criterion, if the overpotential is maintained for 10 h, the catalyst may be suitable for real device fabrication, taking into consideration the catalyst nature and mass loading as well (17). The high activity would manifest itself in a low Tafel slope at real operating potentials. The catalyst specific activity (specific current for electrocatalysis) is the product of the following catalyst characteristics, assuming ideal kinetics with no transport limitations (Equation (i)):

$$\text{Specific activity } [A/g_{Ir}] = \text{Intrinsic activity (TOF)}[A/mol_{\text{active sites}}] * \text{Active/surface site stoichiometry}[mol_{\text{active sites}}/mol_{\text{surface atoms}}] * \text{Ir dispersion}[mol_{\text{surface atoms}}/mol_{\text{Ir total}}] / 192\ [g_{Ir}/mol_{Ir}] \quad \text{(i)}$$

This equation clarifies that it is not enough to develop highly dispersed iridium catalysts, which would be a relatively easy task to do by synthesising sub-2 nm iridium particles with >50% dispersion but that a proper type of iridium species must dominate the surface. Furthermore, the involved parameters must be stable over the device lifetime.

The activity of the catalyst is usually dependant on the OER pathway, which has been shown to depend on the treatment of the iridium catalyst. In general, two mechanisms have been proposed, with the main difference being the predominant involvement of electron-deficient electrophilic oxygen (denoted as $O^{I-}$) and as activated lattice oxygen in the reaction. The OER on rutile-type $IrO_2$ proceeds by means of the classical oxide, electrochemical oxide or electrochemical peroxide pathways involving M–O, M–OH and M–OOH intermediates (18, 19) (Equations (ii)–(vii)):

$$M + H_2O \longrightarrow M\text{-}OH_{ads} + H^+ + e^- \quad \text{(ii)}$$

$$2M\text{-}OH_{ads} \longrightarrow M\text{-}O_{ads} + M + H_2O \quad \text{(iii)}$$

$$M\text{-}OH_{ads} \longrightarrow M\text{-}O_{ads} + H^+ + e^- \quad \text{(iv)}$$

$$2M\text{-}O_{ads} \longrightarrow 2M + O_2 \quad \text{(v)}$$

$$M\text{-}O_{ads} + H_2O \longrightarrow M\text{-}OOH_{ads} + H^+ + e^- \quad \text{(vi)}$$

$$M\text{-}OOH_{ads} \longrightarrow M + O_2 + H^+ + e^- \quad \text{(vii)}$$

where M represents the metal oxide $IrO_2$; the oxide pathway involves reactions (ii), (iii) and (v), the electrochemical pathway involves reactions (ii), (iv) and (v), and the peroxide pathway involves reactions (ii), (iv), (vi) and (vii). The peroxide pathway has recently been shown to provide trends that are in agreement with experimental observations by Schuler *et al*. (19). The electrochemical oxide path is highlighted in red in **Figure 2**.

Catalyst featuring an electrochemically grown porous hydrous oxide layer, also known as oxy-hydroxide layer or amorphous $IrO_x$ catalysts, exhibit an OER mechanism that involves an electrophilic $O^{I-}$ species (21) and an activated lattice oxygen pathway (22, 23). According to Geiger *et al*. (22), a simplified pathway highlighting the need for the

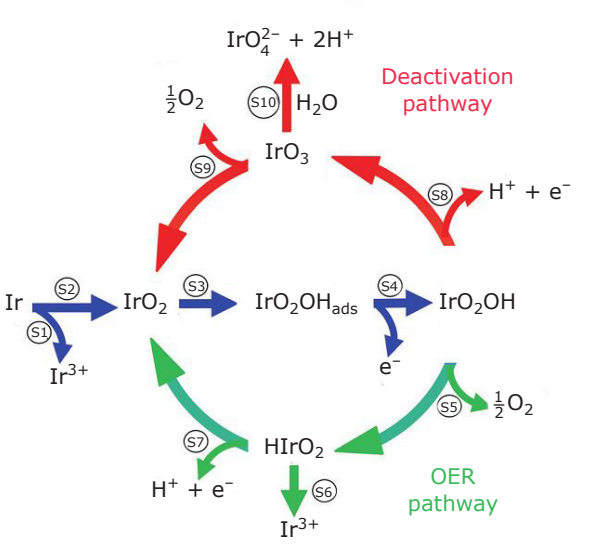


Fig. 2. OER and deactivation pathways in acidic OER, with green route being preferable at lower potentials, red route at higher potentials, while the blue route is potential independent. Reprinted with permission from (20), copyright John Wiley and Sons 2018

outer layer of the catalyst to be involved in the reaction could be Equations (viii)–(x):

$$\text{Ir-x-Ir} + H_2O \longrightarrow \text{Ir-O-Ir} + 2H^+ + 2e^- \quad \text{(viii)}$$

$$\text{Ir-O-Ir} + H_2O \longrightarrow IrO_2 + 2H^+ + 2e^- \quad \text{(ix)}$$

$$IrO_2 \longrightarrow \text{Ir-x-Ir} + O_2 \quad \text{(x)}$$

where x is a vacancy in the porous hydrous oxide layer. Other references have attributed the increased activity to electrophilic $O^{I-}$ species (21). Ir-O-Ir would play a similar role to the proposed highly reactive, electrophilic oxygen $O^{I-}$ species (21, 24). The second step would have a similar function to the preliminary reaction proposed by Pfeifer *et al*. (24) (Equation (xi)):

$$IrO_xO + H_2O \longrightarrow IrO_x\text{-O-O-H} + H^+ + e^- \quad \text{(xi)}$$

where $IrO_xO$ represents the $IrO_2$ matrix with an adsorbed oxygen. The pathway involving the electrophilic $O^{I-}$ species is also highlighted in **Figure 2** in green, where $HIrO_2$ would loosely represent the $O^{I-}$ intermediate.

The OER has been shown to be more active for the pathway involving the electrophilic $O^{I-}$ species and activated lattice oxygen. Unfortunately, this pathway tends to be deactivated due to the lattice oxygen evolution leading to iridium dissolution, and to the transformation of the oxo-hydroxide to less active anhydrous species (22, 25–27). Stabilisation of the iridium atoms in the pathway involving the electrophilic $O^{I-}$ intermediate *via* enhanced crystallinity (26) or the use of mixed oxides could minimise stability issues. Crystalline $IrO_2$ has a lower intrinsic activity but is more stable due to strong Ir–O bonds between $IrO_6$ clusters, with only topmost layers of the rutile contributing to both processes (25). The superior stability of thermal $IrO_2$ is explained by slower kinetics of $IrO_3$ hydrolysis as compared to its decomposition (20). It has been suggested that both pathways occur during the OER with the activated lattice oxygen pathway being dominant at low potential, due to its high activity, and the classical pathway being dominant at higher potential (20). At potentials relevant to the OER, it is possible that the oxo-hydroxide layer slowly transforms to anhydrous oxide with a subsequent loss in activity and enhancement in stability as recently shown by atomic probe tomography (27).

Speaking of which iridium phase is to be synthesised and introduced into the electrochemical device, the literature features metallic iridium with a variety of predominant crystallographic orientations, amorphous hydrous $IrO_2$, crystalline rutile $IrO_2$, their mixtures, as well as multimetallic iridium composites. The metallic iridium may be oxidised by calcination in air before the catalyst layer assembly (28) or electrochemically *in situ* (26, 29). Thermal iridium oxidation to $IrO_2$ occurs between 200°C and 500°C (30), the higher the temperature, the higher the crystallinity and electrochemical stability, but the surface area and the activity decrease (31). The 400–500°C region was recommended to strike a balance between activity, stability and conductivity (28).

Many state-of-the-art catalysts, as shown below, use electrochemical *in situ* oxidation. The iridium (110) surface evolves into two chemically different iridium species, with an active accessible oxide-metal interface (32). The most dense (111) iridium surface is more resistant to the oxidation, and once the oxide is formed, the metallic interface is buried. Although the kinetics of oxide formation and redox properties of the two surfaces are different, their final reached OER activities are rather similar. The same work (32) recommends that for the formation of a porous hydrous $IrO_2$, the *in situ* Ir(0) activation should include oxidising-reducing cycles, instead of conventionally used electrooxidation, although another study argues that the repetitive electrochemical oxidation and reduction unavoidably leads to dissolution (33). The electrochemical oxidation proceeds *via*

 

hydroxide to the irreversible Ir(IV) oxide formation in the nanoparticles, while bulk iridium preserves its metallic subsurface with porous Ir(IV) surface layers (34). Thus, one must be mindful of the iridium dissolution during electrochemical oxidation *via* hydrous $IrO_2$ growth (33). When 20 nm iridium films are used for the acidic OER, their lifetime is similar to the lifetime of the hydrous $IrO_2$ and is significantly lower than for crystalline $IrO_2$ (22).

To produce highly crystalline $IrO_2$, which is more stable but less active than hydrous $IrO_2$, preliminary annealing in air may be recommended, whenever possible. The exceptions, of course, include unsupported polymer-stabilised nanoparticles (26), where annealing would result in particle agglomeration, as well as metal carbides, where it would lead to oxidation and loss of conductivity (35). In such cases, the electrochemical oxidation procedure must be optimised as it affects the catalyst stability.

Fine tuning of the oxide crystallinity, crystallographic orientation, number of oxygen defects and length and strength of Ir–Ir and Ir–O bonds *via* thoughtful synthetic approaches may diminish the gap between the active but unstable and stable but less active phases. Some such examples, leading to state-of-the-art catalysts, are given below.

Thus, the treasure hunt for the most efficient iridium OER catalyst is a simultaneous optimisation of activity *vs*. stability. In addition, in order to achieve high iridium utilisation, the catalyst must be easy to integrate into a catalyst layer in order to yield a layer that has both low loadings, and excellent charge and mass transport. Charge transport should include both electronic and protonic in-plane and through-plane conductivities. Proton transport can be optimised by controlling the amount of electrolyte in the layer (36, 37), while improving electron conductivity can be achieved with the use of a conductive support and interconnected $IrO_x$ network. Similarly, good in-plane conductivity could be maximised by using a porous transport layer (PTL) with a microporous layer (38).

The catalyst lifetime depends on its operating current density and overpotential. It may be estimated using the so-called activity-stability factor (39) or stability number (S-number) (22) i.e. the ratio of evolved oxygen to dissolved iridium at constant overpotential (39). Geiger *et al*. reported that $IrO_2$ powder features a one year lifetime at 200 A $g_{Ir}^{-1}$ *vs*. one month for hydrous oxide (22). The numbers are specific to the used electrochemical cell (**Figure 3**); for example, oxygen bubble accumulation, a common occurrence in rotating disk electrode (RDE), could make the stability studies not a reliable predictor for the catalyst lifetime in a PEM electrolyser long-term behaviour (16). In a PEM electrolyser, iridium dissolution might result in both iridium ions in the water feed, and migration and redeposition at the anode/membrane interface, membrane (40–42) and possible deposition on the cathode leading to platinum deactivation, especially at high current densities and overpotentials (42).

Last but not least, even if the most ideal active and stable iridium phase is developed, the benefits will only manifest if other occurring phenomena are not rate-limiting. The high intrinsic activity and stability may be masked by the limitations in the characterisation technique used, or by the electrode fabrication methodology (43, 44). For example, the commonly used RDE technique might be subject to inert backing passivation (44), and catalyst coated membrane (CCM) fabrication techniques, such as spray-coating, doctor blade and inkjet printing method, could result in very different electrode structures for full-cell testing. Inadequate RDE or CCM fabrication, or non-optimal electrolyte loading can result in excessive charge and mass transport limitations. Further, possible causes of loss of activity are poisoning of the catalyst surface by Nafion™ (45), impurities in the electrolyte in RDE. In the presence of non-iridium components, cations place-exchange with sulfonic acid groups in the polymer electrolyte resulting in decreased proton conductivity (46). All

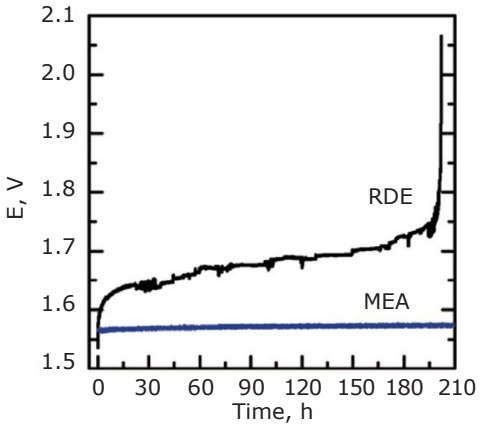


Fig. 3. Evaluation of $IrO_2/TiO_2$ catalyst stability in an RDE and membrane electrode assembly at 70 A $g_{Ir}^{-1}$. Reprinted from (16) under the Creative Commons Attribution License, copyright 2019 The Authors

these complicate not only the scale-up, but also the assessment of the intrinsic catalyst performance in laboratory-scale devices. It is possible that efficient catalysts have not been identified because of these limitations. Some benchmarking procedures for the OER evaluation have been proposed in RDE (26, 47) and alternative liquid-flow (44, 48, 49) or vapour-fed cells (19) and are urgently needed to be followed.

## 3. Synthesis of Unsupported Iridium/$IrO_x$/Ir-OOH Catalysts

### 3.1 Adams' Fusion Method

Adams' method was originally developed to conquer the issues of irreproducible platinum catalyst synthesis; it was successfully scaled up and is used industrially for platinum (Adams') catalyst production (50, 51) and thus is well positioned for potential scalability. It also appears to be one of the most used methods reported for the synthesis of $IrO_2$ for OER, including supported and multimetallic composites. The method is based on the synthesis of iridium nitrate from an iridium molecular precursor heated in a solid mixture with sodium nitrate, followed by the iridium nitrate high-temperature decomposition to $IrO_2$. The side products include poisonous nitrous oxides, which release must be appropriately managed. Synthesis parameters include the temperature and duration of the calcination, nature of the iridium precursor and its fraction in the mixture with $NaNO_3$, all of which affect the crystallinity, oxidation state and surface area of the produced material and thus, the OER performance. The higher is the calcination temperature, the higher is the crystallinity of the produced oxide. However, the amount of active surface hydrous $IrO_2$ decreases, as well as the catalyst surface area. Although the increase in the calcination temperature leads to the lower iridium dispersion (larger particle size) and lower turnover frequency (TOF) due the formation of less active crystalline $IrO_2$, the latter is more stable towards dissolution. This indicates the existence of the optimal calcination temperature to achieve the activity-selectivity balance for the maximised iridium utilisation (31). Electrical conductivity is also improved with increased crystallinity at annealing (52). The highest reported surface area of an $IrO_2$ produced by a modified Adams' method is 350 $m^2\ g^{-1}$, which was obtained from iridium acetylacetonate and calcined in air at 350°C for 30 min (31). The oxide consists of nanodisks with surface partially covered by active Ir(OOH), which however retained only 55% of its activity after 500 potential cycles due to mass loss and restructuring. When the original sample was further heated at 400°C for 1 h, the catalyst retained 70% of its activity after 500 potential cycles. Increased calcination temperature, however, led to a decrease in surface area to 250 $m^2\ g^{-1}$. At the catalyst loading of 0.1 $mg_{IrO_x}\ cm^{-2}$, the specific current of 26 A $g_{IrO_x}^{-1}$ could be achieved at 295 mV overpotential before the stability tests (0.1 M $HClO_4$). For both catalysts, the same activity loss (of 30%) occurred due to the partial oxidation of active sites, but due to the decreased leaching from the 400°C treated sample, the latter strikes the balance between the activity and stability (31). The increase in calcination temperature leads not only to the surface area decrease but also changes the particle morphology to rods with dominating {110} surface terminations (53).

Among other promising reported modifications of Adams' method, the addition of cysteamine to the iridium precursor solution resulted in the formation of $IrO_2$ nanoneedles of 2 nm diameter (6–8 layers of (110) plane, **Figure 4**) and 30 nm length after 450°C calcination (54). Although the needles possessed lower Brunauer–Emmett–Teller (BET) surface area than the catalyst formed without cysteamine (141 $m^2\ g^{-1}$ *vs.* 197 $m^2\ g^{-1}$), their electrical conductivity was six-fold higher. An overpotential of 313 mV was required to achieve 10 mA $cm^{-2}$ at the catalyst loading of 0.21 $mg_{Ir}\ cm^{-2}$ (1M $H_2SO_4$, 25°C) before and after a 2 h durability test. The needles were also tested in a PEM electrolyser and found more active and stable than the spherical $IrO_2$ synthesised without cysteamine (54). Most likely, the less dense and well-connected structure of iridium needles contributed to the improved porosity and electrical conductivity. Thin

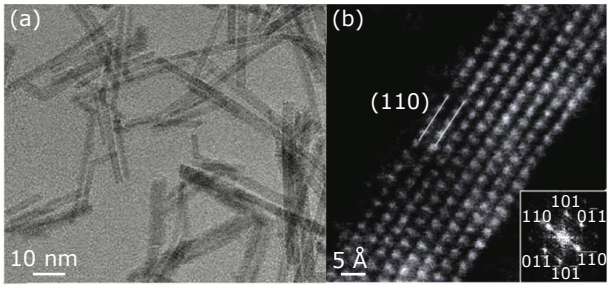


Fig. 4. (a) Ultrathin $IrO_2$ nanoneedles; (b) ultrathin $IrO_2$ nanoneedles consisting of eight (110) layers. Reproduced from (54) with permission from John Wiley and Sons. Copyright 2017

needles with near-zero sphericity form packed beds with the highest near-100% porosity as opposed to 40% for the spherical particles.

## 3.2 Iridium Nanoparticles Stabilised by a Capping Agent

If one has to produce monodisperse near-spherical nanoparticles with high dispersion (>50%, i.e., smaller than *ca*. 2 nm) to increase metal utilisation or form anisotropic nanostructures to increase the catalyst layer porosity or promote the formation of certain crystal terminations, colloidal synthesis in the presence of a capping agent is a popular method in academic research (55). Halogen-containing stabilisers, such as cetyltrimethylammonium bromide (CTAB), are known to act also as a growth-directing agent by the halogen selective adsorption on (100) surfaces resulting in rod-like structures. The produced structures are usually pre-washed from the excess chemicals, while the *in situ* electrochemical preconditioning removes the surfactant, for example, by 50 potential sweeps from 0.05 $V_{RHE}$ to 1.5 $V_{RHE}$ (RHE = reversible hydrogen electrode) (29). Since the metallic iridium is oxidised electrochemically, it is likely to possess a higher proportion of activity-relevant hydrous $IrO_2$ on the surface, as opposed to calcined rutile $IrO_2$.

One of the most successful examples in this category is the 2.0 ± 0.4 nm iridium nanoparticles formed by $IrCl_3$ reduction in ethanol with excess $NaBH_4$ in the presence of CTAB (8). $NaBH_4$ is a strong and fast reducing agent to produce metallic nanoparticles and is often used in the colloidal synthesis. In a protic solvent, borohydride decomposes to gaseous hydrogen, which, depending on the conditions, may proceed in a violent manner. To reach 10 mA $cm^{-2}$ current, *ca*. 290 mV overpotential was required at only 0.061 $mg_{Ir}$ $cm^{-2}$ loading in an RDE (0.5 M $H_2SO_4$, 25°C). The catalyst demonstrated a similar Tafel slope of *ca*. 40 mV $dec^{-1}$ as the calcined catalyst prepared by the Adams' fusion method (31). However, the specific current at 1.51 V was an order of magnitude higher (100 A $g_{Ir}^{-1}$). The nanoparticles formed a nanoporous structure with well-connected particles, which retained their metallic core but featured an active thin surface oxide layer (**Figure 5(a)** and **5(b)**). Authors stressed the importance of complete $IrCl_3$ removal by adding excess of reducing agent to prevent inhibition of electron transfer. Although the catalyst showed an order of magnitude higher specific current than Ir black (Umicore, Belgium) in an RDE, it required only 250 mV lower potential to reach 2 A $cm^{-2}$ current (1.85–1.9 V) when tested in an unoptimised PEM electrolyser with 1 $mg_{Ir}$ $cm^{-2}$ loadings. This again indicates the effect of various factors in a PEM electrolyser.

The use of tetradecyltrimethylammonium bromide (TTAB) during $IrO_2$ precipitation from $H_2IrCl_6$ by NaOH, followed by reduction by $NaBH_4$, resulted in the formation of 1.7 nm metallic iridium seeds that self-assembled into nanodendrites with 34% porosity at 39 $m^2$ $g^{-1}$ BET surface area (29). The high crystallinity favoured stability toward

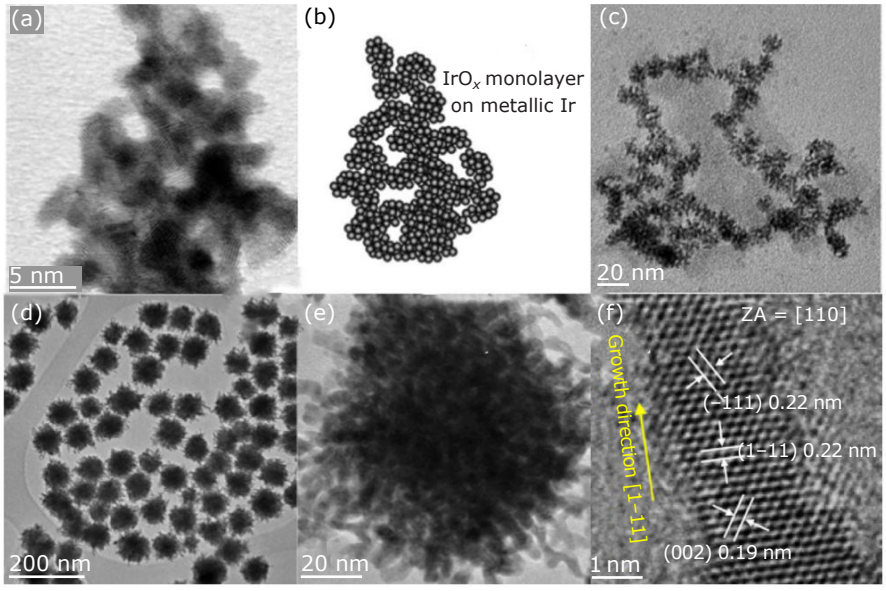


Fig. 5. (a)–(b) Stabilised interconnected iridium nanoparticles (8); (c) iridium nanodendrites (29) (reproduced from (8) and (29) under a Creative Commons Attribution 3.0 Unported License, published by The Royal Society of Chemistry); (d)–(f) highly-crystalline nanopompons (26) (reproduced from (26) under a Creative Commons License, published by Elsevier)

dissolution. The 10 mA $cm^{-2}$ current was achieved at 410 mV overpotential (RDE, 0.05 M $H_2SO_4$) but at only 0.0102 $mg_{Ir}$ $cm^{-2}$ loading. At 1.51 V, the catalyst activity was 70 A $g_{Ir}^{-1}$. Similarly to the CTAB-stabilised particles (8), the formed structure featured high porosity and well-connected individual particles (**Figure 5(c)**).

When a slow reducing agent is used for synthesis (such as glucose (26)), the CTAB suppressed the grain growth in (100) directions; the nanodendrites self-assembled into nanopompons (**Figure 5(d)–(f)**). Those highly crystalline structures with a high proportion of low-index crystal terminations were relatively resistant to dissolution but showed lower activity as compared to the hydrous $IrO_2$ (26).

The stabiliser-assistant synthesis techniques are easy to implement in a wet laboratory without specialised equipment for academic research. This method of iridium synthesis is also used to preform iridium nanostructures prior to their deposition on a support. One must be mindful of a typically low metal concentration in the synthesis solution, the relatively large use of solvents, reductants, stabilisers and washing solutions, many of which are manufactured from fossil resources and expensive. Such synthesis methods are usually too cumbersome for industrial production, the improvements being feasible though for certain stabilisers (56).

### 3.3 Stabiliser-Free Wet Chemical Synthesis Methods

This category features one of the most active catalysts reported to date, although the electrodes were fabricated without Nafion™. Synthesis of 1.6 ± 0.3 nm iridium particles was performed without a stabiliser by heating a solution of $IrCl_3$ in methanol, which reduces $IrO_2$ precipitated by co-added NaOH; the resulting solution was used without purification (9, 57). At a loading of 0.0071 mg $cm^{-2}$ achieved by drop casting of the native solution, the particles formed a uniform layer on a glassy carbon (GC) disk. In 0.1 M $HClO_4$, in an RDE, the catalyst demonstrated an outstanding 205 A $g_{Ir}^{-1}$ activity at 1.5 $V_{RHE}$ and 1130 A $g_{Ir}^{-1}$ at 1.55 $V_{RHE}$ (57). The electrochemically active surface area (ECSA) was found to be 140 $m^2$ $g^{-1}$ (at a loading of 0.0071 $mg_{Ir}$ $cm^{-2}$). The overpotential to reach 10 mA $cm^{-2}$ was 345 mV at 0.0071 $mg_{Ir}$ $cm^{-2}$ loading, or 325 mV at 0.0143 $mg_{Ir}$ $cm^{-2}$ loading (9). The iridium loading on the electrode was of vital importance: loading increase above 0.0071 mg $cm^{-2}$ resulted in significant drop of the ECSA and thus specific current (9). The specific activity at the optimal loading surpasses the activity for the surfactant-mediated catalysts (8), and features a significantly easier, cheaper and scalable preparation. In addition to being surfactant-free and using a low-boiling easily recoverable solvent, the method is scalable to high metal concentrations (5 g $l^{-1}$) (57).The fate of $Na^+$ (10:1 Na:Ir) is to be investigated, as well as the catalyst durability and performance in a PEM electrolyser.

Many studies feature a similar iridium nanoparticle synthesis without a surfactant with the use of a base (NaOH) in other reducing solvents, but typically such particles are deposited on a support, and are discussed in Section 4.

## 4. Wet Synthesis of Iridium Catalysts on Powdered Supports

In heterogeneous catalysis, supports, typically with a high specific surface area, are used to stabilise highly dispersed active metal nanoparticles, both during catalyst synthesis and to ensure their stability against agglomeration during a reaction. In the case of electrolysers, the supports can also be used to enhance the electrode electrical conductivity as they will reduce the contact resistance between particles. The acidic OER environment dictates specific requirements to the type of support: it must be resistant to chemical and electrochemical dissolution, and preferably must have a high electronic conductivity. The latter need is mandatory if iridium loading is low; however, if $IrO_2$ covers most of the support, it may provide sufficient percolative transport for the electrons (3). The film, however, must be as thin as possible to provide advantages over unsupported $IrO_2$ nanoparticles. In this subsection, we focus on the wet synthesis of iridium catalysts on powdered supports, which could be mixed with a Nafion™ solution for catalyst layer preparation.

In recent years, carbon and metal carbides have been receiving less and less attention because of carbon oxidation and volatilisation to $CO_2$ at high applied potentials (58). As a notable exception, one of the most active iridium catalysts reported so far features a carbon-based support (10). A 40 wt% iridium catalyst was prepared by impregnation of graphitic carbon nitride (GCN) nanosheets with the metal precursor followed by annealing in air at 350°C. Thus embedded $IrO_2$ possesses compressed Ir–Ir bonds and decreased coordination numbers of Ir–O and Ir–Ir, which was suggested to weaken the adsorption of oxygen intermediates leading

 

to increased OER activity. The reported specific currents are 580 A $g_{Ir}^{-1}$ at 1.55 V and 1493 A $g_{Ir}^{-1}$ at 1.6 V. The catalyst required the overpotential of 278 mV at 10 mA $cm^{-2}$ at 0.07 $mg_{Ir}$ $cm^{-2}$ loading (in RDE in 0.5 M $H_2SO_4$). Authors demonstrated only 35 mV potential increase at 20 mA $cm^{-2}$ for *ca*. 4 h in an RDE; and 78.5% current retention in a laboratory water splitting device after a 24 h operation at 1.6 V. The fate of GCN was assessed by holding 2.2 $V_{RHE}$ for 2 h with intermediate cyclic voltammetry (CV) measurements between 0.4 $V_{RHE}$ and 0.6 $V_{RHE}$; the double-layer capacitance decreased by 10% in the first 0.5 h and remained stable up to 2 h (10); apparently, the graphitic support nature with nitrogen heteroatom provides its stability in acidic electrolysis. Given the high catalyst activity and a rather easy and potentially scalable preparation of GCN and Ir/GCN, the studies of the catalyst durability and performance in a PEM electrolyser are warranted.

Among oxidation-resistant conductive metal oxide supports, antimony tin oxide (ATO), indium tin oxide (ITO) and fluorine tin oxide (FTO) have been the focus of the most research because of their relatively high conductivity. Unfortunately, the dopant's corrosion brings down the conductivity, increasing ohmic losses and decreasing the energy efficiency (59). Dissolved cations may also ion-exchange with the membrane and lead to its degradation (46). A recent study observed neither activity nor stability benefits from the dopant addition (60). Although FTO possess the lowest conductivity, it was found to be the most stable material between –0.34 $V_{RHE}$ and 2.7 $V_{RHE}$, followed by ITO and ATO. The stability is assigned to the oxygen atom exchange in $SnO_2$ with fluorine, instead of cation exchange in the case of ATO and ITO synthesis (59). ATO, in turn, was suggested to mitigate iridium dissolution by preserving it in lower oxidation states (61). Commercially available samples usually feature low surface areas; several synthetic techniques were suggested in literature for the preparation of mesoporous doped $SnO_2$ with relatively high areas (for example, between 125 $m^2$ $g^{-1}$ and 263 $m^2$ $g^{-1}$) (62). To deal with toxic $NH_4F$ for the FTO synthesis, safety measures must be in place, as in any chemical and engineering process. A number of iridium catalysts supported on doped $SnO_2$ with high activities and low overpotentials at low iridium loadings were recently reported.

A popular method for the preparation of supported iridium OER catalysts is a colloidal precipitation of $IrO_2$ from an iridium molecular precursor by means of NaOH; the synthesis may proceed in ethylene glycol (29), which serves both as a solvent and a reducing agent, or, for example, in a hydrothermal microwave reactor (63). Small 2–3 nm particles may be obtained (61), or even smaller (1.5 ± 0.2 nm) if a stabiliser is added (64). The support may be added to the colloidal dispersion either during synthesis, or after the nanoparticle formation. The use of high-boiling ethylene glycol, though, complicates the potential process scale-up because solvent removal under vacuum is usually used (57), instead of centrifugation or filtration of highly diluted suspensions, as practiced in laboratories. As an example of such preparation method, when $SnO_2$ was doped with tantalum to produce tantalum tin oxide (TaTO) and used to deposit preformed 1.7 nm $IrO_x$ nanoparticles at 11–18 wt% iridium loading, the OER activity of the fresh catalysts after electrochemical conditioning approached 250 A $g_{Ir}^{-1}$ at overpotentials of 280 mV and 370 mV at 0.020 $mg_{Ir}$ $cm^{-2}$ loading (25°C, 0.05 M $H_2SO_4$) (11). Although the electronic conductivity of TaTO was two orders of magnitude lower than that of ATO, its use did not result in decreased activity, which was ascribed to the conducting role of well dispersed $IrO_x$ nanoparticles. In accelerated ageing tests at 1.2–1.6 V potential steps, the $IrO_x$/TaTO catalysts demonstrated between 70% and 90% activity retention *vs*. 60% for the ATO-supported catalyst. The loss of the dopant was one or two orders of magnitude lower for tantalum as compared to antimony, while the loss of tin was not affected. The iridium dissolution was found dependent on the tantalum loading: the higher loading decreased iridium oxidation state contributing to its dissolution, while at lower loadings tantalum shell suppressed $IrO_x$ nanoparticle detachment. This study (11) also demonstrates that the use of a support contributes to enhanced iridium leaching, as compared to commercial $IrO_2$. As a result, although the activity of unsupported $IrO_2$ is significantly lower than that of the developed catalysts, its stability to dissolution contributes to high S-numbers (ratio of evolved oxygen to dissolved iridium) (22). For example the S-number for $IrO_2$ was twice as high as that for selected $IrO_x$/TaTO catalysts at 1.6 V and similar at 1.5 V (11). When hydrous $IrO_x$ was supported on ATO, its S-number was also lower than the one for unsupported $IrO_x$, but the calcined supported samples demonstrated up to two orders of magnitude higher S-number as compared to $IrO_2$ (60).

 

When the above-mentioned (Section 3.2) surfactant-stabilised iridium nanodendrites (39 $m^2$ $g^{-1}$ area) were deposited on high-surface-area ATO (235 $m^2$ $g^{-1}$), an initial overpotential of 260 mV at 10 mA $cm^{-2}$ at only 0.0102 $mg_{Ir}$ $cm^{-2}$ loading (RDE, 0.05 M $H_2SO_4$) was observed while accelerated durability test showed a minor overpotential increase by 30 mV over 15 h compared to an abrupt increase for other tested catalysts at earlier times (29). The specific current at 280 mV overpotential was reported at 70 A $g_{Ir}^{-1}$ *vs*. 8 A $g_{Ir}^{-1}$ for Ir black. In a PEM electrolyser, the catalyst demonstrated the current density of 1.5 A $cm^{-2}$ at 1.8 V and 1 mg $cm^{-2}$ loading compared to 0.8 A $cm^{-2}$ for Ir black.

An atomically dispersed iridium on ITO with ultimate iridium dispersion was developed by grafting 0.86 wt% iridium as an organometallic iridium complex followed by calcination in air at 400°C (65). The specific current of 156 A $g^{-1}$ iridium was reached at 280 mV overpotential and 0.021 $mg_{Ir}$ $cm^{-2}$ loading (0.1 M $HClO_4$). An overpotential of 350 ± 20 mV was required to drive the 10 mA $cm^{-2}$ current at such low metal loadings over the course of 2 h; some iridium agglomeration was observed in the used catalyst and its consequences on the long-term performance requires further analysis.

From the catalyst synthesis viewpoint, one must be mindful that the support's chemical composition may change during the synthesis, affecting the electrochemical performance. For example, if Adams' method involving high-temperature calcination is used to produce $IrO_2$ on a carbide support, the support oxidation leads to the loss of conductivity (for example, TaC lost its conductivity from 120 S $cm^{-1}$ to $10^{-8}$ S $cm^{-1}$ at such circumstances) (35). A similar carbide oxidation to a less-conductive oxide was reported for iridium nanoparticle synthesis in the presence of a support by a polyol method (heating in a reducing ethylene glycol with precipitating NaOH) (58). Moreover, iridium, tin and indium oxides may form mixed oxides; the lattice vacancies are thus produced upon tin and indium *in situ* dissolution, improving the initial activity but jeopardising the durability (66) due to enhanced iridium dissolution.

## 5. Mixed Metal Oxides

Development of multimetallic iridium-containing catalysts has recently attracted considerable attention as a means of enhancing the OER catalyst performance, as had proven beneficial for catalyst development for fuel cells and alkaline water electrolysis. However, with iridium being the most corrosion resistant metal and still dissolving under the acidic OER conditions, any other metal would have an even higher dissolution rate. A rather popular combination of iridium and ruthenium features high activities due to the higher OER activity of ruthenium than that of iridium, but is not practical because of low corrosion resistance of ruthenium, which is also a scarce and expensive metal. The studies of the mixed oxide OER catalysts do typically address (and inevitably show) the dissolution of the catalyst components, but there is a lack of studies on the effect of the leached ions on the PEM system level. It is likely that the non-iridium cations may not only ion-exchange on Nafion™ changing its properties (67), but may also travel to the cathode side and poison the platinum cathode as was shown for iridium (42). Membrane degradation may also occur due to the attack of $HO^{\bullet}$ and other radicals, whose formation is catalysed by transition metal cations (46). For example, iron and copper ions were shown to dramatically enhance membrane degradation (68).

Thus, a practical mixed oxide catalyst for an acidic OER application may be envisioned as one of the following composites (**Figure 6**): (a) an $IrO_x$ shell fully covering the core with an earth-abundant metal increasing the iridium dispersion. In this case, electrolyte contamination with the second metal may be delayed as compared to the mixed alloys until the iridium shell atoms leach exposing the core atoms; (b) iridium nanostructures produced by the preliminary removal of a sacrificial second component from a bimetallic composite, either by potential cycling or chemically. The selective leaching of the second component leads to surface restructuring (69), porosity enhancement (39), formation of lattice vacancies (70) and ECSA increase (71). Lattice vacancies formation *via* secondary metal leaching is a unique opportunity to modify the electrophilicity and Ir–O bond length leading to the enhanced OER activity as compared to $IrO_x$ synthesised only from an iridium precursor (70, 72). Some works report, though, that iridium leaching from the composites may even be increased due to the created lattice vacancies, as compared to monometallic iridium catalysts (39).

Below, we provide some examples for such catalyst synthesis and performance. We note that the direct deposition methods, such as reactive sputtering and physical vapour deposition, are very frequently used for the mixed oxide studies

 

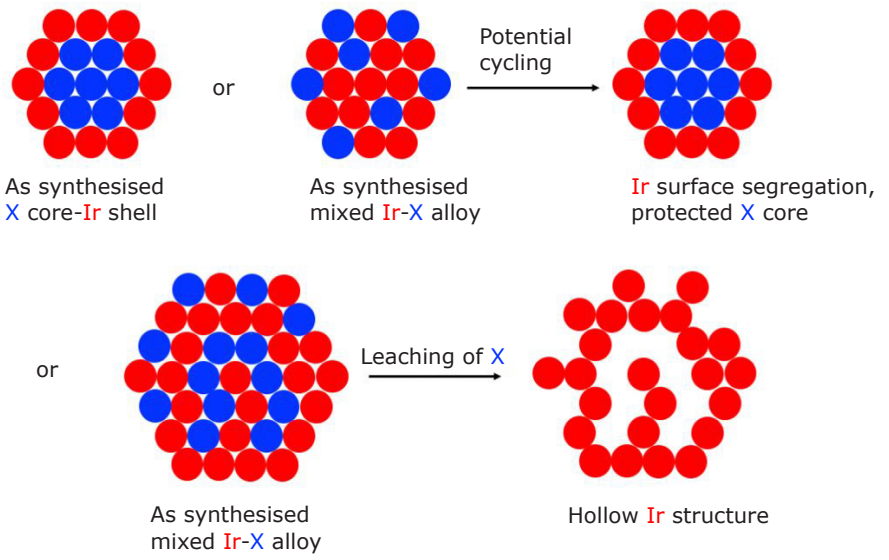


Fig. 6. Mixed metal oxides for the acidic OER catalyst preparation

(39, 71–75), because they ensure structures with well-controlled composition and stoichiometry, thus, enabling the fundamental understanding of the composite's behaviour. As this review does not cover the catalyst layer preparation methods, we only focus on the production of metal oxide powders or colloidal dispersions which were or could be mixed with the Nafion™ solution.

## 5.1 Core-Shell Bimetallic Nanoparticles

Multimetallic composites can be synthesised using all the techniques applicable for monometallic catalyst synthesis (see Section 3) with the addition of the second precursor, with the fine tuning of the reaction conditions. Very often, both precursors are added together during the synthesis. Simultaneous reduction of different ions with different redox potentials leads to the formation of either mixed alloy particles or core/shell nanoparticles (76). For the core-shell synthesis, methods like ionic substitution (galvanic replacement) can be used (77) where a precursor of the second metal is deposited onto the metallic nanoparticles of the other metal based on the standard electrochemical potential (78), or a hydrogen-sacrificial method (79) where a core metal is hydrogenated, followed by the second ion reduction by the surface hydrides and shell formation. It is important to understand that thermodynamically unstable bimetallic structures can be synthesised (in terms of metal distribution) but how fast they rearrange into the thermodynamically stable composites (for example, where a metal with a lower cohesive energy segregates to the surface) depends on temperature, chemical and electrical environment. Metals can even change their location *in situ* depending on the catalysed reaction or treatment conditions *via* so-called adsorbate-induced segregation (80–82). Under the OER conditions, the restructuring may be expected to be an ongoing process with transient equilibrium states due to the different rates of metal dissolution.

According to the Hume-Rothery substitution rule, in order to form a continuous solid solution, it is imperative that the difference between the atomic radii of the solvent and the solute not exceed 15% of each other and they should possess similar crystal structures (83). One of the most common metals alloyed with iridium is ruthenium, but regardless of the efforts being made to inhibit ruthenium leaching, literature report continuous ruthenium dissolution, irrespective of methods of synthesis and structure of the mixed metals oxides. Ruban *et al*. reported a comprehensive table of surface segregation energies in transition-metal alloys, which can help predicting the final dealloyed structure of iridium composites (84). In bimetallic alloys with iridium, metals such as copper, zirconium, rhodium, palladium, silver, hafnium, platinum and gold would segregate to the surface, while iridium would surface-segregate from alloys with titanium, vanadium, chromium, manganese, iron, cobalt, nickel, niobium, molybdenum, technetium, ruthenium, tantalum, tungsten, rhenium and osmium (84). Indeed, for example, in ruthenium-iridium alloys iridium formed a protective shell, offering an extended stability to ruthenium (85).

Another example, conforming to the iridium surface segregation prediction, relates to the iridium-nickel composite. Bimetallic 7 nm $IrNi_{3.2}$ alloy nanoparticles were prepared by a simultaneous reduction of iridium and nickel precursors in the presence of a stabiliser (70). The followed potential cycling from 0.05 $V_{RHE}$ to 1.5 $V_{RHE}$ for 50 cycles resulted in partial nickel leaching, dealloying and oxidation with the formation of a metallic IrNi alloy(core)-$IrO_x$(shell) nanostructure. The $IrO_x$ shells are doped with holes (originated from nickel leaching); they feature shorter Ir–O bonds and are more electrophilic than conventional $IrO_2$, which affects the rate of O–O bond formation during OER and enhanced intrinsic activity per iridium site. A specific current of 676 A $g_{Ir}^{-1}$ was reported at 300 mV overpotential with 0.0102 $mg_{Ir}$ $cm^{-2}$ loading, which is one of the highest in the above presented examples (70). This example shows an extraordinary combination of increased iridium utilisation due to its preferential location in the nanoparticle shell, as well as its beneficial electronic and thus catalytic activity modification upon dealloying.

## 5.2 Selective Leaching of the Sacrificial Component (Hard Templating)

When a secondary metal in bimetallic composites with iridium is selectively removed, the process results in the formation of porous iridium nanostructures with high accessible active site density and modified $IrO_x$ electronic and geometric properties, which cannot be achieved *via* a monometallic iridium catalyst synthesis. Some examples of a sacrificial metal are nickel (12, 86), cobalt (86) and osmium (39). Among different leaching methods, the most common are acid leaching (12) and potential cycling (39, 71). For example, iridium was deposited on nickel nanowires *via* galvanic displacement, followed by the nanowires ('hard template') removal by acid leaching (12). The residual composite with 90.5 wt% iridium demonstrated a specific current of 1650 A $g_{Ir}^{-1}$ at 0.0306 mg $cm^{-2}$ loading at 300 mV overpotential in RDE in 0.1 M $HClO_4$. A parent mixed metal structure can be prepared as stabilised nanoparticles in a colloidal solution, such as an iridium-osmium oxide (39). The potential cycling resulted in dealloying and fast osmium dissolution, leaving behind a nanoporous architecture of iridium metal core and $IrO_x$ shell with an optimised stability and conductivity (39). An important observation was that a high amount of Os–Ir bonds in the parent alloy led to the maximum iridium dissolution upon fast osmium leaching.

This category features some of the most architecturally-sophisticated porous nanostructures, such as hollow nanocrystals synthesised *via* formation of a iridium-cobalt-nickel solid nanoparticles, followed by cobalt and nickel etching with $Fe^{3+}$ (86), or double-layered nanoframes produced in a solution *via* reduction of nickel, copper and two types of iridium precursors with different reduction kinetics followed by acid leaching (87). Theoretically, this approach may produce highly porous connected iridium-only nanostructures, but its practical implementation is complicated by the nuances in the size and structure control, as well as secondary component complete leaching without the structure collapse.

It appears that the main achievement of the selective etching is not in the improvement of iridium surface area and dispersion, as the thus-synthesised catalysts do not feature areas above 100 $m^2$ $g^{-1}$ as compared with monometallic $IrO_2$ synthesised by Adams' method with 250 $m^2$ $g^{-1}$ (31). Instead, the etching allows for modification of the $IrO_x$ electronic structure and vacancies, affecting its OER activity and stability.

## 6. Conclusions

The fast-growing pool of published studies on the iridium-catalysed acidic OER continually contributes to the mechanistic understanding of iridium activity and durability, the role of the second metal in alloys and metal-support interactions. As a myriad of more or less sophisticated methods and structures emerges, one must keep in mind the method practicality, safety, ease and scalability, and that it must use as little resources and produce as little waste as possible. This, most likely, precludes the use of surfactant-assisted routes of wet catalyst synthesis and might jeopardise stabiliser-free colloidal synthesis in vast amounts of organic solvents.

Despite the many advances on catalyst synthesis, and recently proposed metrics to assess catalyst activity and stability, such as the S-number and the activity-stability factor, a lack of consensus on the metrics used to report catalyst performance, as well as the electrochemical testing benchmarking procedures, make the comparison of different catalysts challenging. Activity studies reviewed for the fresh catalysts are not always accompanied by meaningful stability assessment, and high reported activities should be regarded with care,

 

as the most active (hydrous) amorphous $IrO_x$ is less stable than the less active crystalline $IrO_2$. With such considerations, it appears, to our subjective opinion, that Adams' fusion method (or other thermal methods) producing relatively stable rutile, deserve closer attention and further modifications. To take advantage of the enhanced activity of electrophilic oxygen sites, as follows from the multioxide studies, modification of the electrophilicity and Ir–O bond length *via* secondary metal leaching is a possible way to bridge the gap between the activity and stability. The use of supports may increase the stability of the calcined catalysts, however, the addition of dopants to improve electrical conductivity must be used with care.

One must keep in mind that the catalyst layer fabrication can have a tremendous effect on the activity observed in a real electrode. The ionomer-to-catalyst ratio, particle size, the use of a support, catalyst-ionomer-solvent interactions in the dispersion, and deposition technique, can have a significant impact on the electrode electrochemical surface area, ion and electron conductivity and its ability to transport reactant and byproducts in and out of the cell. Gas-phase catalyst synthesis and deposition methods, for example (13), which were not reviewed here, may provide a promising alternative to the wet-chemistry techniques. Moving forward, not only the catalyst synthesis, but also development of common characterisation techniques and metrics to assess activity and stability in RDE, and optimal electrode fabrication methods must become paramount in our collective effort to develop the most efficient OER catalyst, and OER electrode.

## Acknowledgements

As a part of the University of Alberta's Future Energy Systems research initiative, this research was made possible thanks to funding from the Canada First Research Excellence Fund (Grant No. T06-P04).

## References

1. C. Vogt, M. Monai, G. J. Kramer and B. M. Weckhuysen, *Nat. Catal.*, 2019, **2**, (3), 188
2. S. A. Grigoriev, V. N. Fateev, D. G. Bessarabov and P. Millet, *Int. J. Hydrogen Energy*, 2020, **45**, (49), 26036
3. K. A. Lewinski, D. van der Vliet and S. M. Luopa, *ECS Trans.*, 2015, **69**, (17), 893
4. J. Kibsgaard and I. Chorkendorff, *Nat. Energy*, 2019, **4**, (6), 430
5. "The Future of Hydrogen", International Energy Agency, Paris, France, June, 2019
6. C. Wang, F. Lan, Z. He, X. Xie, Y. Zhao, H. Hou, L. Guo, V. Murugadoss, H. Liu, Q. Shao, Q. Gao, T. Ding, R. Wei and Z. Guo, *ChemSusChem*, 2019, **12**, (8), 1576
7. H. Jang and J. Lee, *J. Energy Chem.*, 2020, **46**, 152
8. P. Lettenmeier, J. Majchel, L. Wang, V. A. Saveleva, S. Zafeiratos, E. R. Savinova, J.-J. Gallet, F. Bournel, A. S. Gago and K. A. Friedrich, *Chem. Sci.*, 2018, **9**, (14), 3570
9. F. Bizzotto, J. Quinson, A. Zana, J. J. K. Kirkensgaard, A. Dworzak, M. Oezaslan and M. Arenz, *Catal. Sci. Technol.*, 2019, **9**, (22), 6345
10. J. Chen, P. Cui, G. Zhao, K. Rui, M. Lao, Y. Chen, X. Zheng, Y. Jiang, H. Pan, S. X. Dou and W. Sun, *Angew. Chem. Int. Ed.*, 2019, **58**, (36), 12540
11. S. Abbou, R. Chattot, V. Martin, F. Claudel, L. Solà-Hernandez, C. Beauger, L. Dubau and F. Maillard, *ACS Catal.*, 2020, **10**, (13), 7283
12. S. M. Alia, S. Shulda, C. Ngo, S. Pylypenko and B. S. Pivovar, *ACS Catal.*, 2018, **8**, (3), 2111
13. H. Yu, N. Danilovic, Y. Wang, W. Willis, A. Poozhikunnath, L. Bonville, C. Capuano, K. Ayers and R. Maric, *Appl. Catal. B Environ.*, 2018, **239**, 133
14. J. M. Roller, M. J. Arellano-Jiménez, R. Jain, H. Yu, C. B. Carter and R. Maric, *J. Electrochem. Soc.*, 2013, **160**, (6), F716
15. M. Bernt, A. Siebel and H. A. Gasteiger, *J. Electrochem. Soc.*, 2018, **165**, (5), F305
16. M. Bernt, A. Hartig-Weiß, M. F. Tovini, H. A. El-Sayed, C. Schramm, J. Schröter, C. Gebauer and H. A. Gasteiger, *Chem. Ing. Tech.*, 2020, **92**, (1–2), 31
17. M. Tahir, L. Pan, F. Idrees, X. Zhang, L. Wang, J.-J. Zou and Z. L. Wang, *Nano Energy*, 2017, **37**, 136
18. T. Reier, H. N. Nong, D. Teschner, R. Schlögl and P. Strasser, *Adv. Energy Mater.*, 2017, **7**, (1), 1601275
19. T. Schuler, T. Kimura, T. J. Schmidt and F. N. Büchi, *Energy Environ. Sci.*, 2020, **13**, (7), 2153
20. O. Kasian, J.-P. Grote, S. Geiger, S. Cherevko and K. J. J. Mayrhofer, *Angew. Chem. Int. Ed.*, 2018, **57**, (9), 2488
21. V. A. Saveleva, L. Wang, D. Teschner, T. Jones, A. S. Gago, K. A. Friedrich, S. Zafeiratos, R. Schlögl and E. R. Savinova, *J. Phys. Chem. Lett.*, 2018, **9**, (11), 3154
22. S. Geiger, O. Kasian, M. Ledendecker, E. Pizzutilo, A. M. Mingers, W. Tian Fu, O. Diaz-Morales, Z. Li, T.

 

Oellers, L. Fruchter, A. Ludwig, K. J. J. Mayrhofer, M. T. M. Koper and S. Cherevko, *Nat. Catal.*, 2018, **1**, (7), 508

23. A. Grimaud, A. Demortière, M. Saubanère, W. Dachraoui, M. Duchamp, M.-L. Doublet and J.-M. Tarascon, *Nat. Energy*, 2017, **2**, (1), 16189
24. V. Pfeifer, T. E. Jones, J. J. Velasco Vélez, C. Massué, M. T. Greiner, R. Arrigo, D. Teschner, F. Girgsdies, M. Scherzer, J. Allan, M. Hashagen, G. Weinberg, S. Piccinin, M. Hävecker, A. Knop-Gericke and R. Schlögl, *Phys. Chem. Chem. Phys.*, 2016, **18**, (4), 2292
25. O. Kasian, S. Geiger, T. Li, J.-P. Grote, K. Schweinar, S. Zhang, C. Scheu, D. Raabe, S. Cherevko, B. Gault and K. J. J. Mayrhofer, *Energy Environ. Sci.*, 2019, **12**, (12), 3548
26. X. Tan, J. Shen, N. Semagina and M. Secanell, *J. Catal.*, 2019, **371**, 57
27. T. Li, O. Kasian, S. Cherevko, S. Zhang, S. Geiger, C. Scheu, P. Felfer, D. Raabe, B. Gault and K. J. J. Mayrhofer, *Nat. Catal.*, 2018, **1**, (4), 300
28. S. Geiger, O. Kasian, B. R. Shrestha, A. M. Mingers, K. J. J. Mayrhofer and S. Cherevko, *J. Electrochem. Soc.*, 2016, **163**, (11), F3132
29. H.-S. Oh, H. N. Nong, T. Reier, M. Gliech and P. Strasser, *Chem. Sci.*, 2015, **6**, (6), 3321
30. B. J. Kip, J. Van Grondelle, J. H. A. Martens and R. Prins, *Appl. Catal.*, 1986, **26**, 353
31. M. Povia, D. F. Abbott, J. Herranz, A. Heinritz, D. Lebedev, B.-J. Kim, E. Fabbri, A. Patru, J. Kohlbrecher, R. Schäublin, M. Nachtegaal, C. Copéret and T. J. Schmidt, *Energy Environ. Sci.*, 2019, **12**, (10), 3038
32. E. Özer, C. Spöri, T. Reier and P. Strasser, *ChemCatChem*, 2017, **9**, (4), 597
33. S. Cherevko, S. Geiger, O. Kasian, A. Mingers and K. J. J. Mayrhofer, *J. Electroanal. Chem.*, 2016, **774**, 102
34. T. Reier, M. Oezaslan and P. Strasser, *ACS Catal.*, 2012, **2**, (8), 1765
35. A. V. Nikiforov, C. B. Prag, J. Polonský, I. M. Petrushina, E. Christensen and N. J. Bjerrum, *ECS Trans.*, 2012, **41**, (42), 115
36. M. Bernt and H. A. Gasteiger, *J. Electrochem. Soc.*, 2016, **163**, (11), F3179
37. M. Mandal, M. Moore and M. Secanell, *ECS Trans.*, 2019, **92**, (8), 757
38. T. Schuler, J. M. Ciccone, B. Krentscher, F. Marone, C. Peter, T. J. Schmidt and F. N. Büchi, *Adv. Energy Mater.*, 2020, **10**, (2), 1903216
39. Y.-T. Kim, P. P. Lopes, S.-A. Park, A.-Y. Lee, J. Lim, H. Lee, S. Back, Y. Jung, N. Danilovic, V. Stamenkovic, J. Erlebacher, J. Snyder and N. M. Markovic, *Nat. Commun.*, 2017, **8**, 1449
40. Q. Feng, X.-Z. Yuan, G. Liu, B. Wei, Z. Zhang, H. Li and H. Wang, *J. Power Sources*, 2017, **366**, 33
41. U. Babic, M. Tarik, T. J. Schmidt and L. Gubler, *J. Power Sources*, 2020, **451**, 227778
42. H. Yu, L. Bonville, J. Jankovic and R. Maric, *Appl. Catal. B: Environ.*, 2020, **260**, 118194
43. S. Martens, L. Asen, G. Ercolano, F. Dionigi, C. Zalitis, A. Hawkins, A. Martinez Bonastre, L. Seidl, A. C. Knoll, J. Sharman, P. Strasser, D. Jones and O. Schneider, *J. Power Sources*, 2018, **392**, 274
44. S. Geiger, O. Kasian, A. M. Mingers, S. S. Nicley, K. Haenen, K. J. J. Mayrhofer and S. Cherevko, *ChemSusChem*, 2017, **10**, (21), 4140
45. F. M. Sapountzi, S. C. Divane, E. I. Papaioannou, S. Souentie and C. G. Vayenas, *J. Electroanal. Chem.*, 2011, **662**, (1), 116
46. U. Babic, M. Suermann, F. N. Büchi, L. Gubler and T. J. Schmidt, *J. Electrochem. Soc.*, 2017, **164**, (4), F387
47. C. C. L. McCrory, S. Jung, J. C. Peters and T. F. Jaramillo, *J. Am. Chem. Soc.*, 2013, **135**, (45), 16977
48. I. Spanos, A. A. Auer, S. Neugebauer, X. Deng, H. Tüysüz and R. Schlögl, *ACS Catal.*, 2017, **7**, (6), 3768
49. C. Spöri, J. T. H. Kwan, A. Bonakdarpour, D. P. Wilkinson and P. Strasser, *Angew. Chem. Int. Ed.*, 2017, **56**, (22), 5994
50. L. B. H., *Platinum Metals Rev.*, 1962, **6**, (4), 150
51. R. Adams and R. L. Shriner, *J. Am. Chem. Soc.*, 1923, **45**, (9), 2171
52. E. Rasten, G. Hagen and R. Tunold, *Electrochim. Acta*, 2003, **48**, (25–26), 3945
53. D. F. Abbott, D. Lebedev, K. Waltar, M. Povia, M. Nachtegaal, E. Fabbri, C. Copéret and T. J. Schmidt, *Chem. Mater.*, 2016, **28**, (18), 6591
54. J. Lim, D. Park, S. S. Jeon, C.-W. Roh, J. Choi, D. Yoon, M. Park, H. Jung and H. Lee, *Adv. Funct. Mater.*, 2018, **28**, (4), 1704796
55. N. Semagina and L. Kiwi-Minsker, *Catal. Rev.: Sci. Eng.*, **51**, (2), 2009
56. P. T. Witte, P. H. Berben, S. Boland, E. H. Boymans, D. Vogt, J. W. Geus and J. G. Donkervoort, *Top. Catal.*, 2012, **55**, 505
57. J. Quinson, S. Neumann, T. Wannmacher, L. Kacenauskaite, M. Inaba, J. Bucher, F. Bizzotto, S. B. Simonsen, L. Theil Kuhn, D. Bujak, A. Zana, M. Arenz and S. Kunz, *Angew. Chem. Int. Ed.*, 2018, **57**, (38), 12338
58. F. Karimi and B. A. Peppley, *Electrochim. Acta*, 2017, 246, 654
59. S. Geiger, O. Kasian, A. M. Mingers, K. J. J. Mayrhofer and S. Cherevko, *Sci. Rep.*, 2017, **7**, 4595

 

60. G. C. da Silva, S. I. Venturini, S. Zhang, M. Löffler, C. Scheu, K. J. J. Mayrhofer, E. A. Ticianelli and S. Cherevko, *ChemElectroChem*, 2020, **7**, (10), 2330
61. H.-S. Oh, H. N. Nong, T. Reier, A. Bergmann, M. Gliech, J. Ferreira de Araújo, E. Willinger, R. Schlögl, D. Teschner and P. Strasser, *J. Am. Chem. Soc.*, 2016, **138**, (38), 12552
62. H.-S. Oh, H. N. Nong and P. Strasser, *Adv. Funct. Mater.*, 2015, **25**, (7), 1074
63. C. Massué, V. Pfeifer, X. Huang, J. Noack, A. Tarasov, S. Cap and R. Schlögl, *ChemSusChem*, 2017, **10**, (9), 1943
64. D. Lebedev and C. Copéret, *ACS Appl. Energy Mater.*, 2019, **2**, (1), 196
65. D. Lebedev, R. E. Ezhov, J. Heras-Domingo, A. Comas-Vives, N. Kaeffer, M. Willinger, X. Solans-Monfort, X. Huang, Y. Pushkar and C. Copéret, *ACS Cent. Sci.*, 2020, **6**, (7), 1189
66. M. Ledendecker, S. Geiger, K. Hengge, J. Lim, S. Cherevko, A. M. Mingers, D. Göhl, G. V. Fortunato, D. Jalalpoor, F. Schüth, C. Scheu and K. J. J. Mayrhofer, *Nano Res.*, 2019, **12**, (9), 2275
67. S. Shi, A. Z. Weber and A. Kusoglu, *Electrochim. Acta*, 2016, **220**, 517
68. T. Kinumoto, M. Inaba, Y. Nakayama, K. Ogata, R. Umebayashi, A. Tasaka, Y. Iriyama, T. Abe and Z. Ogumi, *J. Power Sources*, 2006, **158**, (2), 1222
69. C. Spöri, P. Briois, H. N. Nong, T. Reier, A. Billard, S. Kühl, D. Teschner and P. Strasser, *ACS Catal.*, 2019, **9**, (8), 6653
70. H. N. Nong, T. Reier, H.-S. Oh, M. Gliech, P. Paciok, T. H. T. Vu, D. Teschner, M. Heggen, V. Petkov, R. Schlögl, T. Jones and P. Strasser, *Nat. Catal.*, 2018, **1**, (11), 841
71. O. Kasian, S. Geiger, M. Schalenbach, A. M. Mingers, A. Savan, A. Ludwig, S. Cherevko and K. J. J. Mayrhofer, *Electrocatalysis*, 2018, **9**, (2), 139
72. L. C. Seitz, C. F. Dickens, K. Nishio, Y. Hikita, J. Montoya, A. Doyle, C. Kirk, A. Vojvodic, H. Y. Hwang, J. K. Norskov and T. F. Jaramillo, *Science*, 2016, **353**, (6303), 1011
73. A. W. Jensen, G. W. Sievers, K. D. Jensen, J. Quinson, J. A. Arminio-Ravelo, V. Brüser, M. Arenz and M. Escudero-Escribano, *J. Mater. Chem. A*, 2020, **8**, (3), 1066
74. A. L. Strickler, R. A. Flores, L. A. King, J. K. Nørskov, M. Bajdich and T. F. Jaramillo, *ACS Appl. Mater. Interfaces*, 2019, **11**, (37), 34059
75. O. Kasian, S. Geiger, P. Stock, G. Polymeros, B. Breitbach, A. Savan, A. Ludwig, S. Cherevko and K. J. J. Mayrhofer, *J. Electrochem. Soc.*, 2016, **163**, (11), F3099
76. N. Toshima, *Pure Appl. Chem.*, 2000, **72**, (1–2), 317
77. C. Wang, Y. Sui, G. Xiao, X. Yang, Y. Wei, G. Zou and B. Zou, *J. Mater. Chem. A*, 2015, **3**, (39), 19669
78. B. Coq and F. Figueras, *J. Mol. Catal. A: Chem.*, 2001, **173**, (1–2), 117
79. H. Ziaei-Azad and N. Semagina, *ChemCatChem*, 2014, **6**, (3), 885
80. F. Tao, M. E. Grass, Y. Zhang, D. R. Butcher, J. R. Renzas, Z. Liu, J. Y. Chung, B. S. Mun, M. Salmeron and G. A. Somorjai, *Science*, 2008, **322**, (5903), 932
81. X. Liu, A. Wang, L. Li, T. Zhang, C.-Y. Mou and J.-F. Lee, *J. Catal.*, 2011, **278**, (2), 288
82. K. J. J. Mayrhofer, V. Juhart, K. Hartl, M. Hanzlik and M. Arenz, *Angew. Chem. Int. Ed.*, 2009, **48**, (19), 3529
83. C. Felix, T. Maiyalagan, S. Pasupathi, B. Bladergroen and V. Linkov, *Int. J. Electrochem. Sci.*, 2012, **7**, (12), 12064
84. A. V. Ruban, H. L. Skriver and J. K. Nørskov, *Phys. Rev. B*, 1999, **59**, (24), 15990
85. N. Danilovic, R. Subbaraman, K. C. Chang, S. H. Chang, Y. Kang, J. Snyder, A. P. Paulikas, D. Strmcnik, Y. T. Kim, D. Myers, V. R. Stamenkovic and N. M. Markovic, *Angew. Chem. Int. Ed.*, 2014, **53**, (51), 14016
86. J. Feng, F. Lv, W. Zhang, P. Li, K. Wang, C. Yang, B. Wang, Y. Yang, J. Zhou, F. Lin, G.-C. Wang and S. Guo, *Adv. Mater.*, 2017, **29**, (47), 1703798
87. J. Park, Y. J. Sa, H. Baik, T. Kwon, S. H. Joo and K. Lee, *ACS Nano*, 2017, **11**, (6), 5500


## The Authors

Himanshi Dhawan completed her Bachelor's in Technology in Chemical Engineering from India. In January 2019, she started her PhD at the University of Alberta, Edmonton, Canada where she is currently working on developing iridium based electrocatalysts for OER in acidic media.

 

Marc Secanell is a Professor in the Department of Mechanical Engineering at the University of Alberta. His research focuses on multiscale numerical modelling of electrochemical systems, such as the development of the open-source fuel cell simulation toolbox (openFCST), and the experimental fabrication, characterisation and testing of polymer electrolyte fuel cell and electrolyser electrodes.

Natalia Semagina is a Professor in the Department of Chemical and Materials Engineering at the University of Alberta. Her research focuses on experimental heterogeneous catalysis, controlled synthesis of mono- and bimetallic nanoparticles and elucidation of a catalyst's structure-activity relationship in a variety of applications.